



Integrated CO₂ capture and photocatalytic conversion by a hybrid adsorbent/photocatalyst material



Lianjun Liu^a, Cunyu Zhao^a, Jinye Xu^a, Ying Li^{a,b,*}

^a University of Wisconsin-Milwaukee, Mechanical Engineering Department, Milwaukee, WI 53211, USA

^b Texas A&M University, Department of Mechanical Engineering, College Station, TX 77843, USA

ARTICLE INFO

Article history:

Received 17 February 2015

Received in revised form 2 June 2015

Accepted 4 June 2015

Available online 6 June 2015

Keywords:

CO₂ capture and reduction

Photocatalysis

TiO₂

Layered double oxides

FTIR

ABSTRACT

Carbon dioxide (CO₂) capture and storage (CCS) is costly mainly due to the high energy demand to regenerate the CO₂ sorbents. Photocatalytic reduction of CO₂ is one of the promising routes in CO₂ conversion and utilization (CCU) but is hurdled by its very low conversion. This work, for the first time, integrates CO₂ capture and photocatalytic conversion (CCPC) by using a novel hybrid adsorbent/photocatalyst (TiO₂ nanoparticles supported on MgAl layered double oxides, i.e., MgAl(LDO)/TiO₂), with CO₂ adsorption, desorption and conversion to C1 products operated near power plant flue gas temperatures (100–200 °C). The proportions of desorption and conversion of the captured CO₂ could be manipulated by tuning the reaction temperature, the atomic ratio of adsorbent to photocatalyst, and the dispersion and crystallinity of TiO₂ particles. Experimental results show that the hybrid MgAl(LDO)/TiO₂ not only has a much higher CO₂ capture capacity than bare MgAl(LDO) and TiO₂, but also converts 13–15% CO₂ to carbon monoxide (CO) with a 93–95% overall self-regeneration rate during five adsorption/conversion/regeneration cycles. In situ diffuse reflectance infrared Fourier transform spectroscopy (DRIFTS) analyses have demonstrated that photo-illumination can activate and convert the strongly adsorbed species that cannot be achieved by thermal desorption alone at the same temperature. The novel CCPC process, with further advancement in the materials and reaction design, may provide a competitive alternative to the current carbon management technologies.

© 2015 Elsevier B.V. All rights reserved.

1. Introduction

The continuous increase of the emissions of carbon dioxide (CO₂) from the combustion of fossil fuels are predicted to produce large impacts on the global climate. To address this grand challenge, one viable option to control CO₂ emissions is CO₂ capture and sequestration (CCS) [1–4]. The CCS approach involves three distinct processes: (1) capturing CO₂ from power plants or other large emission sources, (2) transporting the captured CO₂ by pipeline or in tankers, and (3) injecting CO₂ underground for enhanced oil recovery or in deep saline aquifers or unmineable coal seams [1,3,5]. Besides the long-term uncertainty of the carbon sequestration in geological formations, a major challenge in the CCS is to develop advanced, cost-effective, and regenerable sorbents for CO₂ capture. Currently, the common sorbents are either liquids (e.g., amine), solids (e.g., calcium oxide), or amine anchored on

solids (e.g., silica) [2,3,6]. Amine-based wet process warrants a high CO₂ capture capacity, but it includes several disadvantages such as low absorption temperature (~50 °C), high cost for regenerating amine solution, and undesirable solvent reactions with certain compounds in flue gas [4,7–9]. Calcium-based solid sorbents can operate through in situ cyclic carbonation–calcination reactions [10–12]. However, the very high temperatures of CO₂ adsorption (600–800 °C) and CaO regeneration (1000–1100 °C) result in intensive energy consumption and cause the drop-off in capacity due to sorbent sintering and attrition [2,11–13].

To overcome the drawbacks in amine- or calcium-based sorbents, a new class of solid inorganic materials, i.e., magnesium–aluminium layered double hydroxides (MgAl-LDH), has been developed to directly work at flue gas or near flue gas temperature [14–20]. LDH, also known as a hydrotalcite-like compound, consists of stacked layers of brucite [Mg(OH)₂] in which partial Mg²⁺ cations are substituted by Al³⁺ cations at the center of octahedral sites of the hydroxide sheets. The excess positive charge of the brucite-like layers is compensated by anions (CO₃²⁻, HCO₃⁻) in the interlayer space, where water molecules were also located. Especially, the layer double oxides (LDO), derived

* Corresponding author at: University of Wisconsin-Milwaukee, Mechanical Engineering Department, Milwaukee, WI 53211, USA. Fax: +1 979 845 3081.

E-mail address: yingli@tamu.edu (Y. Li).

from thermal dehydration, decarbonation, and dehydroxylation of LDH, are suitable for CO_2 capture at a wide temperature range (150–350 °C) because of more basic adsorption sites exposed. MgAl(LDO) has demonstrated good CO_2 adsorption capacity and reversibility, but compared with amine and zeolite sorbents it has a slightly lower CO_2 capture capacity (<1 mmol/g) [16,18,20,21], and it still requires a relatively high temperature (400–500 °C) to fully regenerate the spent MgAl(LDO) [17,18].

Recent developments of CO_2 conversion and utilization (CCU) make it a more attractive alternative to CCS as CCU not only recycles CO_2 but also produces fuels or value-added chemicals. Particularly, much attention has been paid to catalytic conversion of CO_2 into fuels via thermal decomposition [22], reforming with methane to syngas [23], hydrogenation to methanol [24], and electrocatalytic reduction [25]. Despite of the relatively high conversion efficiency, these catalytic reactions are conducted at either a very high temperature (>700 °C) or a high pressure (50–100 bar). Alternatively, photocatalytic reduction of CO_2 with H_2O has emerged as a promising option, because it offers a green route to recycle CO_2 back to renewable fuels using sunlight at a mild temperature and pressure [26–29]. Titanium dioxide (TiO_2) as a photocatalyst has been extensively studied for CO_2 photoreduction, but the typical CO_2 conversion is very low (below 1%) [26,29,30]. Besides the well-known reasons of fast electron–hole ($e^- - h^+$) recombination and limited harvest of visible light by TiO_2 (wide band gap 3.2 eV for anatase) [27,30–33], some other reasons may be accounted for the low conversion but are seldom addressed, including (1) weakened CO_2 adsorption (an important preceding step for CO_2 conversion) on TiO_2 in the presence of H_2O vapor, and (2) limited desorption of products or intermediates from TiO_2 surface when the photoreaction is conducted at room or near-room temperature [31,32,34–37]. A solution is to increase surface basicity of TiO_2 by adding basic metal oxides like MgO [35,38,39]. Although the photo-conversion of CO_2 has been boosted, the CO_2 adsorption capability of MgO/ TiO_2 is limited due to the low concentration of MgO (<5 wt%), and a higher MgO concentration inhibits CO_2 photoreduction. On the other hand, MgAl(LDO) has advantages over MgO because of better structural stability, higher surface basicity and faster CO_2 adsorption kinetics [40]. Moreover, TiO_2 nanoparticles could be anchored on the surface of MgAl(LDO). Till now, no study has been done to use MgAl(LDO) as both a sorbent for capturing CO_2 and a support for dispersing TiO_2 photocatalysts.

To date, CCS and CCU are usually studied separately in different research communities. The CCU approaches typically use pure or pre-concentrated CO_2 as the feed (as opposed to from diluted sources such as power plant flue gas or ambient), and thus, the CO_2 capture step is still anticipated for large scale CCU operations, significantly increasing the cost of CCU. In this work, we propose a new, more practical and more energy efficient approach that integrates CO_2 capture and photocatalytic conversion (CCPC) near flue gas temperatures, using a novel hybrid adsorbent/photocatalyst material (TiO_2 nanocrystals dispersed on the surface of MgAl(LDO)), i.e., MgAl(LDO)/ TiO_2 . In this unique approach, as shown in Fig. 1, the hybrid material first adsorbs CO_2 at a typical flue gas temperature (ca. 150 °C) and in a second step the adsorbed species (mainly carbonates and bicarbonates) desorb to gas-phase CO_2 while a significant portion is converted to CO under photo-irradiation at a temperature (in the range of 100–200 °C) similar to the adsorption temperature; the hybrid material itself is automatically regenerated (due to both CO_2 desorption and conversion) and ready for the next CCPC cycle. The fraction of the products from CO_2 conversion versus desorbed CO_2 depends on the material composition (ratio of MgAl(LDO) to TiO_2), desorption/conversion temperature, and UV intensity. Advantages of this CCPC approach and the hybrid material are apparent. First it is simple by using only one multi-functional solid material and is suitable for power plant carbon

capture under flue gas temperature (1 atm and 150 °C). Second, the CO_2 conversion and sorbent regeneration temperature is low (less than 200 °C) and thus the waste heat from flue gas plus the solar radiation may be sufficient to provide the thermal energy needs, minimizing the total energy consumption from fossil sources. Also, the UV source for catalytic CO_2 conversion could directly come from sunlight. Finally the CCPC process produces valuable by-products such as CO that can offset the energy cost and capital investment over a long term. Hence, the overall cost of the CCPC process is likely lower than traditional carbon capture processes.

2. Experimental

2.1. Materials synthesis

The chemicals used for materials synthesis are bis(ammoniumlactate) dihydroxide (TALH) (50 wt% in solution, Sigma), urea (>98%, Sigma), $\text{Mg}(\text{NO}_3)_2$ (99.9%, Sigma), $\text{Al}(\text{NO}_3)_3$ (>98%, Sigma), NaOH (99.1%, Fisher scientific), Na_2CO_3 (99.9%, Sigma) and commercial TiO_2 (P25) nanopowder (Nippon Aerosil Co., Japan). The hybrid MgAl(LDO)/ TiO_2 material was prepared by thermally annealing MgAl(LDH)/ TiO_2 that was prepared by hydrothermal synthesis of TiO_2 nanocrystals first and subsequently co-precipitation of MgAl precursors in the TiO_2 colloidal. Briefly, to prepare anatase TiO_2 , 10 ml TALH aqueous solution and a desired amount of 0.1 M urea were mixed followed by the addition of distilled water to reach a final volume of 100 ml. The resulting solution was transferred into a Teflon-lined autoclave, which was sealed and placed in an electric oven held at 160 °C for 24 h. Then, the autoclave was naturally cooled in air. The precipitates were separated by centrifugation, washed with distilled water until pH 7, and dried overnight at 60 °C in an oven.

To prepare MgAl(LDH)/ TiO_2 , in a beaker A, a desired amount of TiO_2 , $\text{Mg}(\text{NO}_3)_2$ and $\text{Al}(\text{NO}_3)_3$ were dispersed in 50 ml H_2O (Solution A). We adjusted the atomic ratio of MgAl(LDO) to TiO_2 (i.e., Mg:Al:Ti = 3:1:1.5, 3:1:3, 3:1:4.5) to explore the optimum composition that warrants both a good CO_2 capture capacity and a high CO_2 conversion. In a beaker B, NaOH (0.08 mol) and Na_2CO_3 (0.008 mol) were dissolved in 50 ml H_2O (Solution B). Subsequently, solution B was slowly transferred into solution A till pH 9 under vigorously stirring. After aging at 70 °C overnight, the precipitate was collected, washed by distilled water till pH 7, and dried at 80 °C overnight to produce MgAl(LDH)/ TiO_2 , which was finally calcined at 400 °C for 5 h to obtain MgAl(LDO)/ TiO_2 . The synthesized hybrids were denoted as MgAl/Ti_x, where x is the nominal atomic percentage of Ti calculated from the fraction of Ti/(Mg + Al + Ti). For comparison, the physical mixture of MgAl(LDO) and TiO_2 (P25) (i.e., MgAl + nTi₄₃(P25)) was also prepared by mechanically grounding the two powdered materials in a mortar.

2.2. Materials characterization

The crystal structures of the catalyst samples were identified by X-ray diffraction (XRD, Scintag XDS 2000) using $\text{Cu K}\alpha$ irradiation at 45 kV and a diffracted beam monochromator at 40 mA. Scanning electron microscopy (SEM) (Hitachi S4800) was used to obtain the surface morphology. The real near surface and bulk concentration of Mg, Al, Ti, and O elements was analyzed by energy dispersive X-ray spectroscopy (EDS) and neutron activation analysis (NAA), respectively. NAA is a nuclear process, where the sample is bombarded by neutrons, causing the elements to form radioactive isotopes. NAA is a highly sensitive technique to determine the bulk concentration of elements (error within 5%). The lattice structure of MgAl(LDO)/ TiO_2 was visualized by phase-contrast high resolution transmission electron microscopy

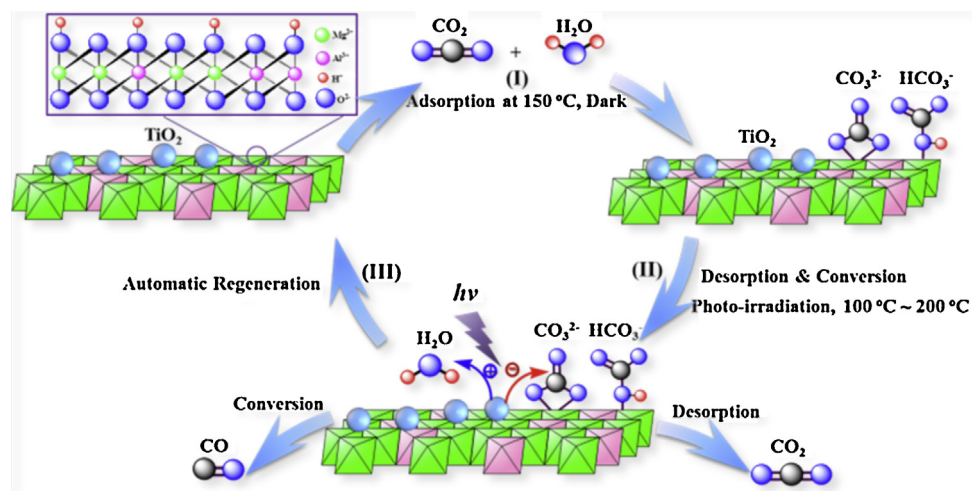


Fig. 1. Schematic of the integrated CO₂ capture and photocatalytic conversion (CCPC) approach using a hybrid adsorbent/photocatalyst (i.e., MgAl(LDO)/TiO₂).

(HRTEM) carried out with 300 keV electrons in a Hitachi H9000NAR instrument with 0.18 nm point and 0.11 nm lattice resolution. The specific surface area and pore volume were analyzed by nitrogen adsorption–desorption at 77 K using the Brunauer–Emmett–Teller (BET) method (Micromeritics, ASAP 2020). The CO₂ adsorption capacity was measured by thermogravimetric analysis (TGA, SDT 2960). CO₂ capture was conducted at 150 °C (close to the flue gas temperature in coal-fired power plants) in the presence of H₂O vapor for 2 h. To eliminate ambient adsorbed CO₂ and moisture when the materials were stored in an air environment, the samples were *in situ* pretreated by helium (He) at 400 °C for 1 h prior to CO₂ capture at 150 °C. After the temperature cool down to the target 150 °C for 10 min, a mixture of CO₂ + H₂O vapor was introduced into the cell in a continuous flow mode. The CO₂ adsorption isotherms were then recorded as a function of time.

2.3. CO₂ capture and photocatalytic conversion

The CO₂ capture and photocatalytic conversion with H₂O vapor was conducted in a home-made quartz tube reactor operating in a continuous flow mode. For each test, 50 mg catalyst was used and evenly dispersed onto a glass-fiber filter that was placed at the center of a photoreactor. Right before CO₂ capture and conversion, the materials were pretreated by helium (He) at 400 °C for 1 h to remove surface adsorbed species from ambient. Two 250 W infrared (IR) lamps were used to heat up the reactor to designated temperatures and by adjusting the distance of IR lamps to the reactor, the temperature can be varied and maintained at a certain level. A 100 W mercury vapor lamp was used as the photo-excitation source, and the light intensity is about 10 mW/cm² in the UV range (<390 nm) (see the spectrum in Fig. S1). The experiments were then conducted in three sequential steps: adsorption, purging, and desorption/conversion. First, CO₂ (99.999%, Praxair) (120 ml/min) continuously passed through a water bubbler to bring a CO₂ + H₂O gas mixture into the reactor at 150 °C for 2 h. Second, the reactor was cooled down (IR lamps off) to room temperature, after which the gas was switched to He + H₂O at a high flow rate to purge out CO₂ out of the reactor and then the flow rate was maintained at 4.5 ml/min. Third, the mercury vapor and IR lamps were turned on simultaneously to desorb and convert the captured CO₂ at designated temperatures (100, 150, or 200 °C). The gaseous products in the reactor effluent were continuously analyzed by a gas chromatograph (GC, Agilent 7890A) equipped with a thermal conductivity detector (TCD) and flame ionization detector (FID). Samples were taken at a 15 min interval.

2.4. *In situ* DRIFTS for CO₂ adsorption/desorption/conversion

All IR spectra were recorded on a Nicolet 6700 spectrometer (Thermo Electron) equipped with a liquid nitrogen cooled HgCdTe (MCT) detector. The spectra were displayed in absorbance units, and acquired with a resolution of 4 cm⁻¹, using 32 scans. The DRIFTS studies were performed in a Praying Mantis DRIFTS accessory and a reaction chamber (Harrick Scientific, HVC-DRP). The reaction cell is equipped with a heater and a temperature controller, as well as a sample cup in the center. The dome of the DRIFTS cell has two KBr windows allowing IR transmission and a third (quartz) window allowing transmission of irradiation introduced through a liquid light guide (Newport) that connects to a 450 W Xe lamp (Oriel).

Prior to the adsorption/desorption, the samples were purged by helium (He) for 1 h at 400 °C to clean the catalyst surface. The temperature was then cooled down to 150 °C, and the background spectrum in the presence of the sample was collected. Next, FTIR spectra were recorded as a function of time to investigate the dynamics of the reactants (e.g., CO₂ and H₂O) adsorption in the dark and desorption/conversion under UV–vis irradiation.

3. Results and discussion

3.1. Crystal structure and morphology of MgAl(LDO)/TiO₂

All the MgAl/Ti_x samples maintained a high crystallinity of TiO₂ in anatase phase (see supplementary Fig. S2). The MgAl-rich MgAl/Ti₂₇ displayed stronger diffraction peaks of MgO crystals than in Ti-rich MgAl/Ti₅₃, while no crystalline Al₂O₃ were observed, probably because Al species were amorphous or doped into MgO lattices by replacing partial Mg²⁺ ions [18,40]. SEM analysis was carried out to explore the morphology of MgAl/Ti_x and MgAl(LDO). The SEM images in Fig. 2a–d shows that all the MgAl/Ti_x samples exhibited a cotton-like morphology. Taking MgAl/Ti₄₃ as an example, the higher magnification SEM image (Fig. 2c) clearly shows relatively uniform nanoplates (~50 nm) that overlap to form multilayer aggregates. Unlike MgAl/Ti₄₃, pure MgAl(LDO) (Fig. 2e–f) consisted of many ultrathin layers (size >100 nm and thickness <8 nm). Obviously, the incorporation of TiO₂ changed the morphology and size of MgAl(LDO), probably because TiO₂ nanoparticles suppressed the growth of MgAl thin layers and induced their aggregation and stacking during the precipitation process.

TEM and HRTEM were conducted to further explore the lattice structure, morphology and TiO₂ dispersion. The TEM image (Fig. 3a) shows that MgAl/Ti₄₃ is composed of nanolayers (about

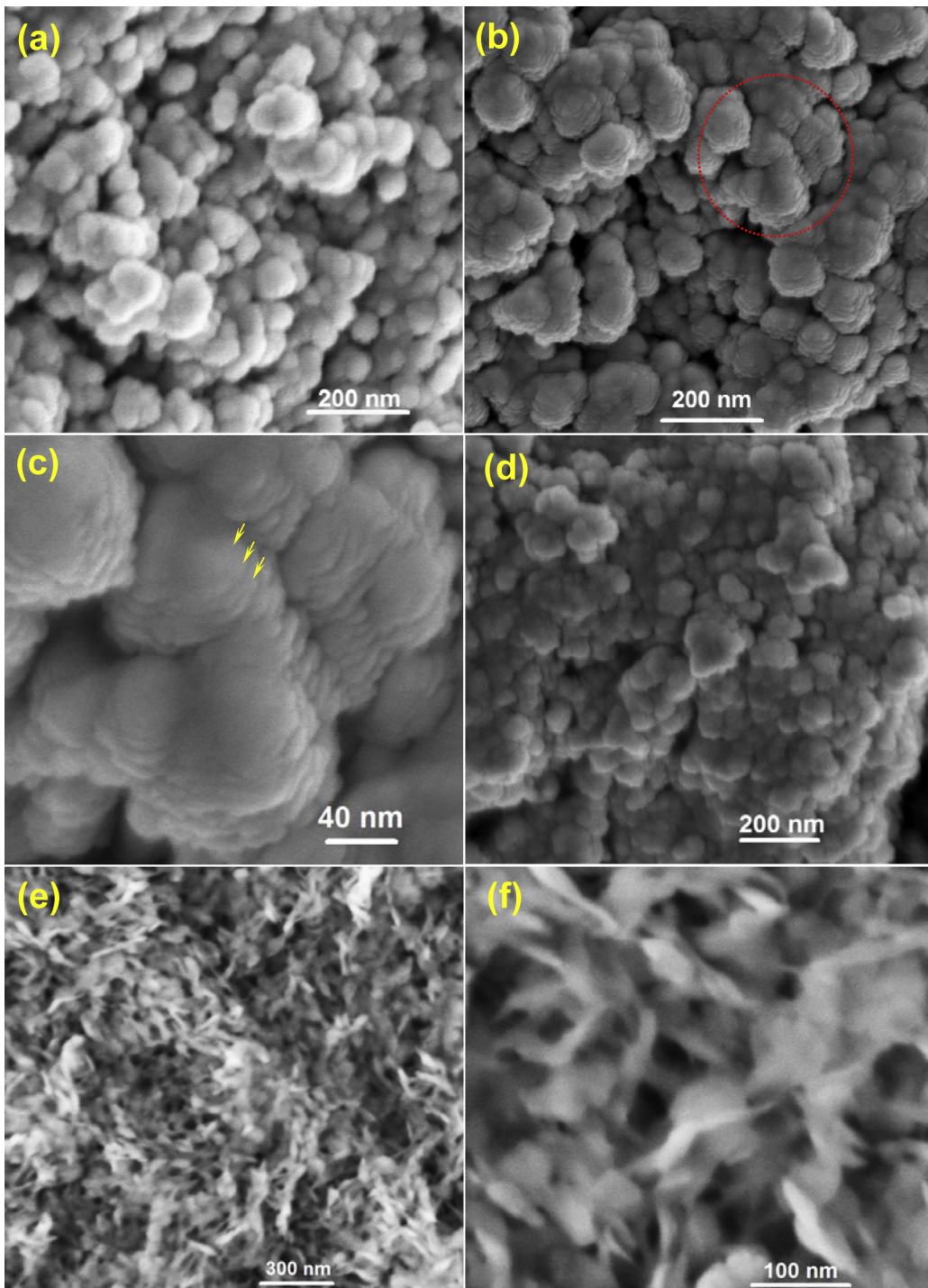


Fig. 2. SEM images of (a) MgAl/Ti₂₇, (b, c) MgAl/Ti₄₃, (d) MgAl/Ti₅₃, and (e, f) MgAl(LDO)

50 nm, side view) and nanoparticles (less than 10 nm). The HRTEM image (Fig. 3b) clearly shows well-faceted nanocrystals with an average size of 7 nm are well-dispersed on the surface of MgAl(LDO) nanoplates (top view). The interplanar spacing around 0.34 nm matches the (1 0 1) plane of TiO₂ anatase phase [32,41,42]. The dispersion of TiO₂ is further explained by the measurement of the relative content of Mg, Al and Ti elements using the EDS and NAA. The EDS results indicated that the real near-surface atomic ratio of Ti/(Ti + Mg + Al) was 71% for MgAl/Ti₄₃, much higher than the nominal or bulk ratio at 43%; while the NAA results indicated the real bulk ratio of Ti/(Ti + Mg + Al) is 38%, very close to the nominal ratio

of 43%. The combined EDS and NAA results suggest that TiO₂ particles were primarily dispersed near the surface of MgAl(LDO) rather than embedded into the matrix.

The textural properties of MgAl/Ti₄₃ and MgAl(LDO) have also been studied by N₂ physical-sorption. The two materials both displayed typical type-IV isotherms (corresponding to the characteristics of mesoporous structure) but different types of hysteresis loops and pore size distributions (PSDs) (see Fig. S3). MgAl(LDO) shows a type H₃ hysteresis loop, suggesting slit-shaped mesopores that are probably caused by the space of the aggregates of thin layers. The PSDs of MgAl(LDO) also shows a sharp peak at 3.4 nm and a

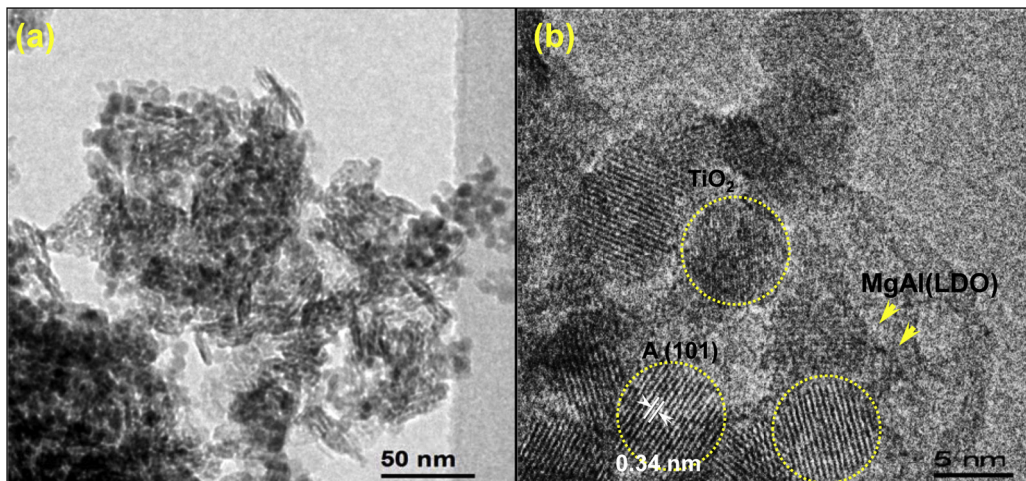


Fig. 3. (a) TEM and (b) HRTEM images of MgAl/Ti₄₃.

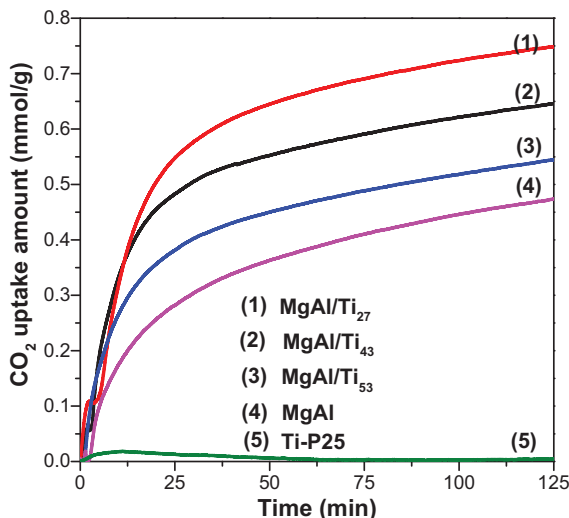


Fig. 4. The TGA isotherms for CO₂-uptake capacity on the TiO₂(P25), MgAl(LDO), and various MgAl(LDO)/TiO₂ samples conducted at 150 °C in the presence of H₂O vapor.

broad one centered at 11.5 nm. By contrast, MgAl/Ti₄₃ shows a type H₂ hysteresis loop and narrowed PSD peaks located at 3.8 nm and 7.5 nm. Clearly, TiO₂ nanoparticles introduced more and smaller mesopores in between MgAl layers, probably resulted from the space between the aggregated nanoparticles and the compacted plates. The addition of TiO₂ to MgAl(LDO) has also significantly increased the BET specific surface area and pore volume (see Table S1). The surface area of MgAl/Ti₄₃ is 242 m²/g, compared with 41 and 57 m²/g for MgAl(LDO) and TiO₂(P25), respectively, probably resulted from the small size of TiO₂ nanoparticles (7 nm) and the presence of smaller mesopores in MgAl/Ti₄₃. The above textural properties analyses were well correlated with SEM and TEM results.

3.2. CO₂ capture and conversion

The CO₂ capture capacity of MgAl/Ti_x was measured by TGA. Fig. 4 shows the CO₂ adsorption isotherms in the presence of H₂O at 150 °C. A two-stage adsorption process is observed for all the MgAl/Ti_x materials, in agreement with the literature on the mechanism of CO₂ adsorption on MgAl(LDH)-derived oxides [16,17,43,44]. In the first stage, fast adsorption occurred over a

relatively short time period (e.g., 0–20 min), because this process was likely dominated by CO₂ diffusion within the MgAl/Ti_x and the weak interaction of CO₂ with OH sites [14,15,43–45]. At a later stage, the CO₂ uptake amount increased in a continuous but slower rate, which may be due to the formation of strongly bound carbonates (e.g., CO₂ coordination with unsaturated O^{2–}) [43,44]. At around 2 h, the net CO₂ adsorption capacity was in the order of MgAl/Ti₂₇ (0.752 mmol/g) > MgAl/Ti₄₃ (0.648 mmol/g) > MgAl/Ti₅₃ (0.534 mmol/g) > MgAl (0.475 mmol/g) > TiO₂(P25) (0.025 mmol/g). Clearly, incorporating TiO₂ with MgAl(LDO) significantly enhanced CO₂ capture capacity (e.g., MgAl/Ti₄₃ has a capacity 24 times higher than that of TiO₂(P25)), demonstrating that MgAl(LDO) can serve as an adsorbent and compensate the limited CO₂ adsorption on TiO₂. Surprisingly, the CO₂ capture capacity of MgAl/Ti₄₃ hybrid was even higher than bare MgAl(LDO). By correlating with N₂ adsorption–desorption isotherms, SEM and TEM/HRTEM results, the enhanced capacity is likely because of the interaction between MgAl(LDO) and TiO₂ nanoparticles, the increased surface area and pore volume, and the formed multilayered structure. These three structural characteristics may have provided more surface adsorption sites and space to accommodate more CO₂ molecules. This is another unique advantage of this hybrid material that has not been reported before.

As shown in the HRTEM image (Fig. 3b), in the MgAl/Ti₄₃ sample, TiO₂ nanoparticles (7 nm) are highly dispersed on the surface of MgAl(LDO) plates. The nanoscale structure introduces particular interactions that is different from bulk interaction between MgAl(LDO) and TiO₂. To verify that, we have conducted a control experiment by physically mixing MgAl(LDO) and TiO₂(P25) (i.e., MgAl + Ti₄₃(P25)) and comparing its CO₂ capture ability. The results show that MgAl/Ti₄₃ has higher CO₂ adsorption capacity (0.648 mmol/g) than the physical mixture of MgAl + Ti₄₃(P25) (0.501 mmol/g), suggesting a stronger interaction between MgAl(LDO) and TiO₂ in the MgAl/Ti₄₃ hybrid material. In addition, we have conducted FTIR to identify the possible chemical bonds in MgAl/Ti₄₃. As shown in Fig. S4, the hydroxyl group on MgAl(LDO) is located at 3613 cm^{–1} and the hydroxyl groups on TiO₂ are at 3719 cm^{–1}/3674 cm^{–1}, while those OH groups on MgAl/Ti₄₃ are at 3549 cm^{–1} and 3656 cm^{–1}. Such red shift in peak positions of OH groups indicates possible formation of new chemical bonds between MgAl and Ti species, i.e., Ti–OH–MgAl. The exact nature of such bonds is subject to future investigation.

The contribution of water vapor to CO₂ adsorption has also been explored by conducting a control experiment of dry CO₂ (without

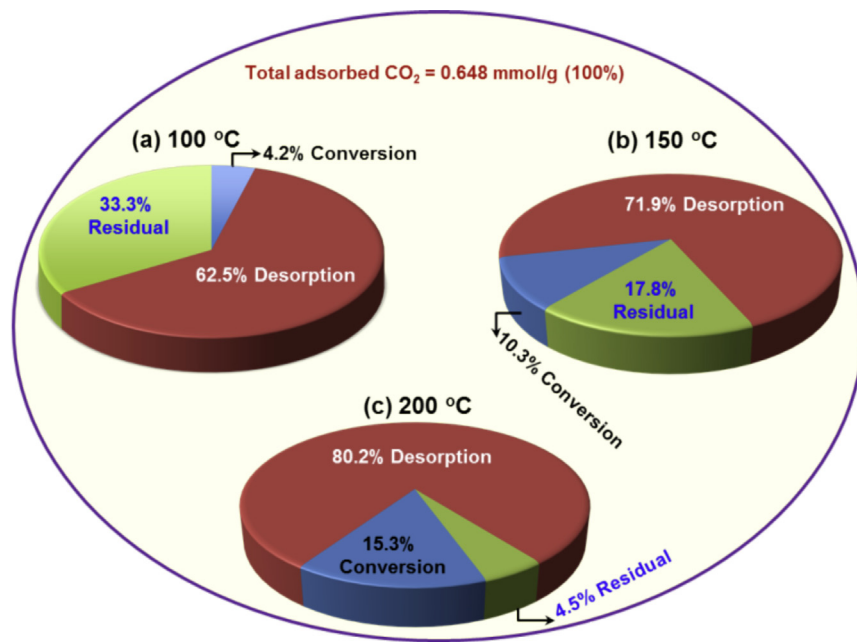


Fig. 5. The proportion of desorbed CO₂, converted CO₂ to CO, and residual carbonates on MgAl/Ti₄₃ at different desorption/conversion temperatures (100 °C, 150 °C, or 200 °C). CO₂ was adsorbed at the same temperature 150 °C; the desorption/conversion process was in the presence of He + H₂O vapor at 4.5 SCCM and under UV irradiation. The concentrations of produced CO and desorbed CO₂ were continuously monitored by GC so that the total amounts can be calculated. Typically the first 2 h accounted for 90% CO₂ desorption capacity and 42% CO₂ conversion capacity; but the process was lasted to a maximum of 16 h till no CO₂ desorption or conversion was detected. Higher carrier gas flow rate or application of vacuum will reduce the time needed for desorption and conversion in real applications.

H₂O) adsorption on MgAl/Ti₄₃. As shown in Fig. S5, the adsorption patterns of wet CO₂ and dry CO₂ look similar with the majority of the adsorption (75–90%) taking place at the beginning 30 min, while at a later stage the weight increase in wet CO₂ increased relatively faster than in dry CO₂. At around 2 h, CO₂ capture capacity in wet CO₂ (0.648 mmol/g) was 45% higher than that in dry CO₂ (0.443 mmol/g). The results suggest that presence of water vapor did not greatly influence the CO₂ adsorption rate but had a promotional impact on the overall CO₂ capture capacity of MgAl/Ti₄₃. This is likely because the oxides react with water vapor to form magnesium and aluminum hydroxides, which could provide additional sites to coordinate with CO₂ to form bicarbonates [46,47].

Once CO₂ capture process was finished, the reactor was cooled down to room temperature and a mixture of He + H₂O vapor was introduced into the reactor to purge out gas phase CO₂, so that we can eliminate the interference of residual gaseous phase CO₂ on the desorption/conversion of the captured CO₂. Subsequently, the CO₂ photocatalytic conversion process started by turning on the UV irradiation while the reactor was simultaneously heated by two infrared (IR) lamps to the designated desorption/conversion temperature (100 °C, 150 °C or 200 °C). CO was found to be the major product from the reduction of adsorbed CO₂, while only a very small amount of CH₄ (two orders of magnitude smaller than that of CO) was produced. The product selectivity was in agreement with our previous study [36,38,39] and the literature reports [32,35]. Because the CH₄ production was negligible compared with that of CO, in this paper, only the production of CO was used to calculate the CO₂ conversion rate. To exclude the thermal-induced catalytic effect and the possibility of surface organic contaminants that may induce CO production, background tests at each of the reaction temperature (100 °C, 150 °C, or 200 °C) were conducted by introducing He + H₂O vapor to the reactor in the presence of the MgAl/Ti_x materials that did not undergo CO₂ capture process. No matter in the dark or under UV irradiation, the amount of CO produced was either not detectable or two order of magnitude lower than that produced when the MgAl/Ti_x material was subjected to CO₂ capture. This con-

firms that the produced CO was indeed derived from photocatalytic conversion of the captured CO₂. In addition, pure MgAl(LDO) was subjected to UV irradiation after CO₂ capture, and only a very small amount of CO was generated (equivalent to 5% of that produced by MgAl/Ti₄₃). This suggests that TiO₂ serves as the main photocatalyst to convert the adsorbed CO₂ to CO.

Generally, the adsorbed CO₂ on the MgAl/Ti_x surface existed as carbonates and bicarbonate, as evidenced by in situ DRIFTS described later in this paper. Upon IR heating and UV irradiation, part of the carbonates/bicarbonate was converted to CO (conversion), part of them was released as gas phase CO₂ (desorption), and the rest remained on the surface (residual). The percentages of conversion (C%), desorption (D%), and residual (R%) were calculated according to the following three equations:

$$C\% = \frac{[\text{ProducedCO}]}{[\text{AdsorbedCO}_2]} \times 100\% \quad (1)$$

$$D\% = \frac{[\text{DesorbedCO}_2]}{[\text{AdsorbedCO}_2]} \times 100\% \quad (2)$$

$$R\% = 100\% - C\% - D\% \quad (3)$$

We found that desorption/conversion temperature is an important factor governing C% and D% of the captured CO₂. As shown in Fig. 5, increasing the temperature from 100 to 200 °C promoted the D% by nearly 30% while significantly enhanced C% by nearly 3 times. Surface carbonates were almost completely removed at 200 °C (only 4.5% residuals). The temperature-dependent enhancement on CO₂ desorption and conversion is in agreement with our previous results using MgO/TiO₂ [38], and the possible reason is that a higher temperature promotes the kinetics of surface intermediates desorption and conversion to CO.

Besides the temperature effect, the material composition (the ratio of adsorbent/photocatalyst) can also influence C% and D%. Fig. 6a compares the performance of various MgAl/Ti_x samples under the same condition (adsorption temperature = 150 °C; desorption/conversion temperature = 200 °C). An increase in Ti atomic

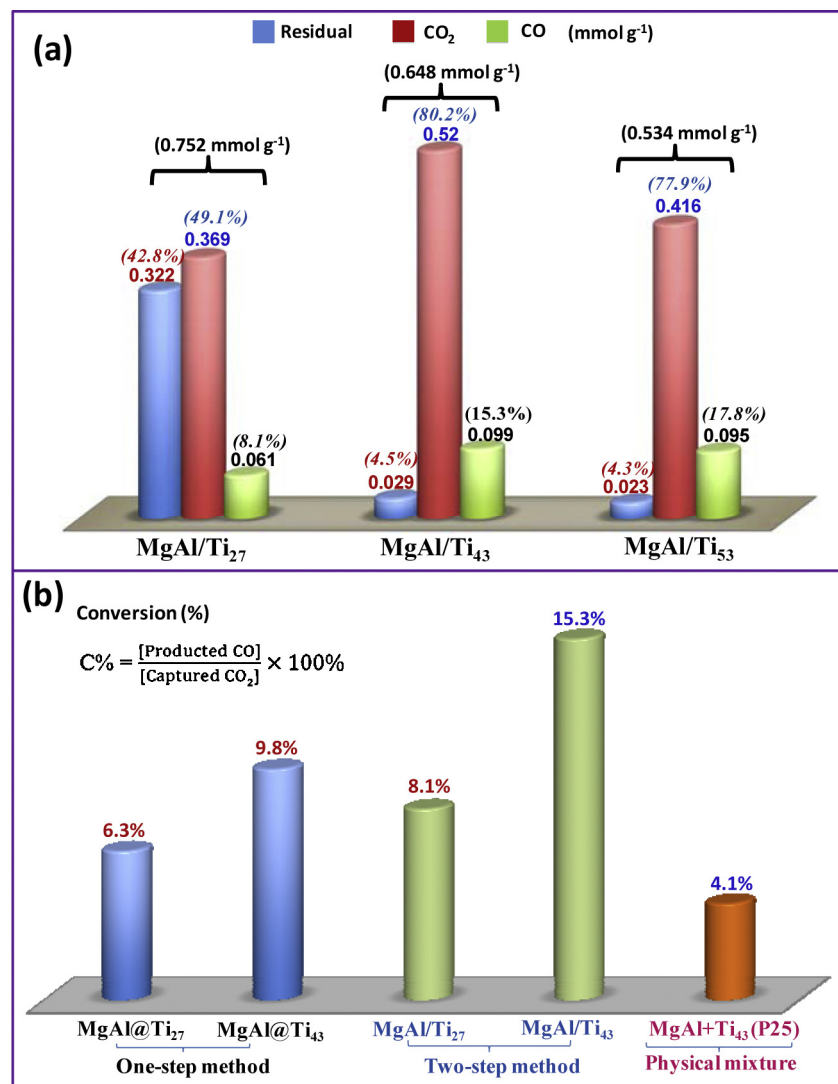


Fig. 6. (a) The concentration and the proportion of residual carbonates, desorbed CO₂, and CO produced from the adsorbed CO₂ on various MgAl/Tix samples under UV irradiation at 200°C, and (b) the percentages of CO₂ conversion to CO on various samples of MgAl/Tix, MgAl@Ti_x, and MgAl+Ti₄₃(P25).

percentage generally resulted in a decrease in the total CO₂ adsorption capacity, which agrees with the fact that MgAl(LDO) is the major adsorption site. MgAl/Ti₄₃ is apparently superior to MgAl/Ti₂₇ because of the much improved C% and D%. However, further increasing Ti ratio to 53% (i.e., MgAl/Ti₅₃) only led to a slight enhancement on C%, while the absolute amount of desorbed CO₂ and produced CO was lower than MgAl/Ti₄₃, probably because MgAl/Ti₅₃ has a lower CO₂ capture capacity than MgAl/Ti₄₃. Hence, there is a trade-off between CO₂ capture and CO₂ conversion capabilities induced by the adsorbent (MgAl-LDO) and photocatalyst (TiO₂) components, respectively. It appears that in this work MgAl/Ti₄₃ has the optimum composition, which has good CO₂ capture capacity and conversion efficiency as well.

We also found that the materials structure is an important factor in governing the CO₂ conversion. The materials characterization results in Figs. 2 and 3 and S2 have demonstrated that MgAl/Tix hybrids have well-dispersed and highly crystallized TiO₂ nanoparticles on the MgAl(LDO) surface. To confirm that this unique structure is the reason for the superior performance in CO₂ desorption and conversion, another set of samples with similar materials composition but different structures were used as a comparison. Those samples were prepared by a physical mixing method (i.e., MgAl+Ti₄₃(P25)) and a conventional one-

pot co-precipitation method (labelled as MgAl@Ti_x, to distinguish from MgAl/Tix previously described). MgAl@Ti_x only produced amorphous TiO₂ species embedded in the MgAl(LDO) (see supplementary Fig. S6). MgAl+Ti₄₃(P25) has the layer structure and high crystallinity of TiO₂, but the interaction between MgAl(LDO) and TiO₂(P25) is weak, thus leading to the lowest C% (4.1%) (see Fig. 6b). MgAl@Ti₄₃ still maintained a mesoporous and thin layered structure, but it has lower C% (9.8%) than that of MgAl/Ti₄₃ (15.3%). The above comparison results suggest that higher crystallinity and well-dispersion of TiO₂ nanoparticles result in stronger interaction with MgAl(LDO) and thus may inhibit the surface and volume electron-hole recombination [33]. The enhanced charge separation can facilitate the electron migration to catalyst surface to activate and convert the adsorbed CO₂, as evidenced by in situ DRIFTS described later in this paper.

3.3. Regeneration and cycling performance

From the data in Fig. 6a, one can easily find that most of the adsorbed carbonates/bicarbonate were either desorbed or converted to CO on MgAl/Ti₄₃ and MgAl/Ti₅₃ (only 4~5% residual on the surface). This is an original finding that for the first time reveals a new route to easily regenerate the materials by integrating photo-

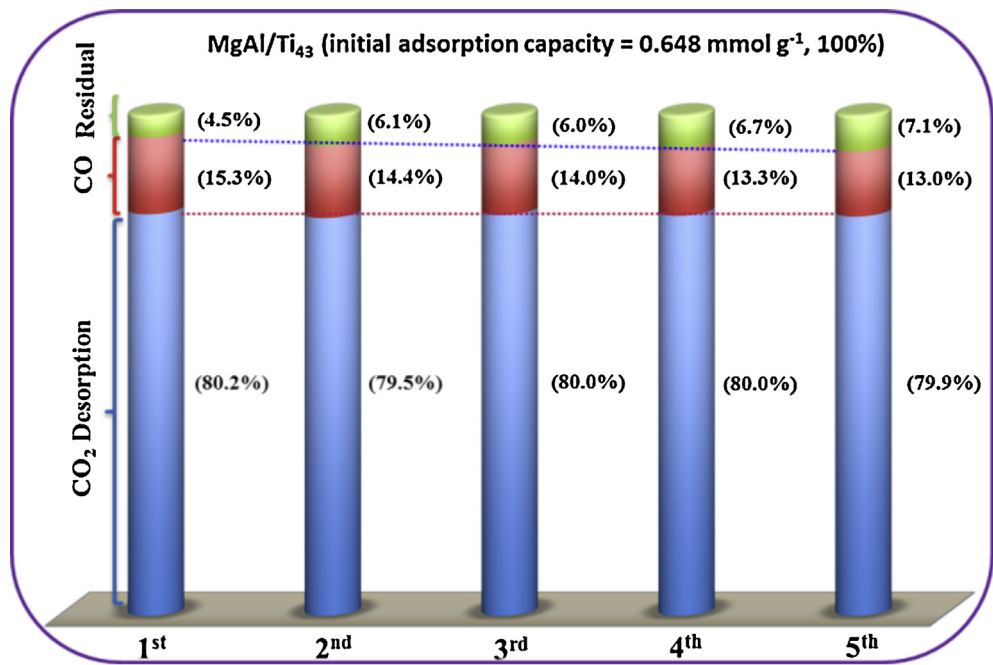


Fig. 7. The cycling performance (three runs) of MgAl/Ti₄₃ under UV irradiation at 200 °C: the percentage of residual carbonates, desorbed CO₂, and produced CO are compared in each cycle.

catalytic effect at a relatively low temperature (200 °C) as oppose to a higher temperature (400–500 °C) typically required in a conventional thermal-regeneration method. Another benefit of this CCPC technology is the production of valuable compounds like CO (a component of syngas which can be processed to liquid fuels). A 15% CO₂ conversion means 15% less CO₂ will be sequestered in a CCS process and equivalent molar amount of CO can be produced as a valuable by-product.

To understand the regeneration ability of the hybrid material by CCPC, we measured the cycling performance of MgAl/Ti₄₃ undergone five runs of adsorption & desorption/conversion alternations. Fig. 7 compares the percentages of desorbed CO₂, produced CO, and residual carbonates in each cycle, assuming the CO₂ adsorption capacity in the 2nd–5th cycle was the same as in the 1st cycle. After five cycles, the D% in the 5th run (79.9%) was comparable to the 1st run (80.2%), and the C% slightly dropped but still maintained as high as 13%. The sum of C% and D% in the 5th cycle (92.9%) is only reduced by 3% from the 1st cycle (95.5%), suggesting that MgAl/Ti₄₃ has a high regeneration capacity. Again, this good cycling performance demonstrated that besides generating useful products (e.g., CO), our CCPC technology offers a facile and low-cost way to recover the CO₂ adsorption ability of the materials as well.

3.4. Separation of desorbed CO₂ and produced CO and the effect of photo-irradiation

The simultaneous CO₂ desorption and conversion process will produce a mixture of CO₂ and CO, with CO being a minor component (see Fig. 8, Condition I). In practical applications, additional processes and energy are needed to separate CO from CO₂. To lower the cost, it is desirable to produce concentrate CO directly. During the CO₂ desorption and conversion process, we found that the rate of CO₂ desorption was much faster than that of photocatalytic conversion. Hence, we anticipate that the desorbed CO₂ and produced CO could be separated by conducting the desorption (thermal effect) and conversion (photocatalytic effect) processes sequentially rather than simultaneously. To verify this hypothesis, an additional experiment was conducted using the MgAl/Ti₄₃ under

such a condition (Condition II): thermal desorption at 200 °C in the dark first for 2 h to completely remove the weakly adsorbed CO₂, and subsequently introducing UV light (still at 200 °C) to convert the residual species. The result shows that the majority of adsorbed CO₂ (72%) was released by thermal effect in the dark process; while during the photo-illumination process, a small portion of additional CO₂ desorbed (11.3%), and in the meantime some adsorbed species were converted to CO (12.7%). Clearly, more concentrated CO gas (CO/CO₂ ratio greater than 1) can be produced under Condition II, which will be more economic than Condition I which produces lean CO gas.

In addition, to prove the concept that this CCPC technology can be used for power plant flue gas treatment, we used diluted CO₂ (10.0% in He) as the feed gas, and the result is shown in Fig. 8, Condition III. Similar percentages and amounts of desorbed CO₂ and produced CO were observed to those under Condition II. When 10% CO₂ was used as the feed gas, it took twice amount of time (4 h) to reach the similar level of adsorption capacity (0.659 mmol/g) to that when pure CO₂ was used (see supplementary Fig. S5), but the adsorption kinetics in the first 20 min were very similar. Hence, most experiments in this work were conducted using pure CO₂ to shorten the total adsorption time, but the reported performance data will still be representative to near-real flue gas applications. Again, the results here demonstrate the potential feasibility of treating CO₂ in the power plant flue gas using this CCPC technology where CO₂ consists 10–20% of the volume fraction in flue gas. The effects of other flue gas components such as SO_x and NO_x on the CCPC performance remain unknown at this point and will be investigated in our future work.

From Fig. 8 we can find that the CO production under Condition II (desorption and conversion sequentially) is lower than under Condition I (desorption and conversion simultaneously), and additional CO₂ was desorbed under Condition II upon UV irradiation after the thermal desorption process. The results revealed that photo-illumination has two distinct functions: (1) enhancing CO₂ desorption that cannot achieve by thermal effect at the same temperature; (2) activating and converting either weakly or strongly adsorbed CO₂ species through photo-generated electrons. This con-

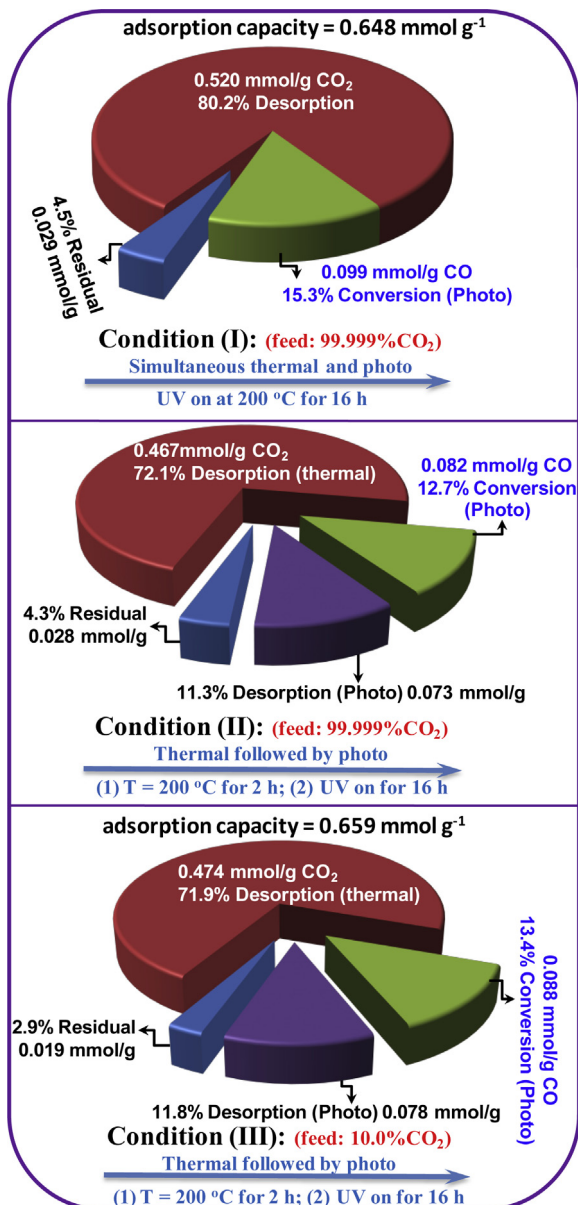


Fig. 8. The amount and the portion of residual carbonates, desorbed CO_2 , and produced CO on MgAl/Ti₄₃ at different conditions. (I): after 99.999% $\text{CO}_2 + \text{H}_2\text{O}$ adsorption for 2 h, UV irradiation at 200 °C simultaneously (left pie); (II): after feeding 99.999% $\text{CO}_2 + \text{H}_2\text{O}$ adsorption for 2 h, desorption at 200 °C first in the dark for 2 h and then under UV light irradiation (middle pie); (III): the procedure was similar to condition (II) but using 10.0% CO_2 for adsorption for 4 h (right pie).

clusion was further supported by in situ DRIFTS analyses (details described later in this paper) that thermal effect alone (200 °C) only induced the desorption of the weakly adsorbed species (part of bicarbonates and bidentate carbonates), while subsequent photo-illumination is able to further activate the strongly bonded species (monodentate carbonate and residual bidentate carbonates).

3.5. In situ DRIFTS for CO_2 adsorption/desorption/conversion

In situ DRIFTS was conducted to monitor the CO_2 capture and conversion process and identify the surface intermediates. The in situ DRIFTS analysis was carried out in four sequential steps in a continuous-flow mode. First, CO_2 capture on the sample surface was studied by introducing a $\text{CO}_2/\text{H}_2\text{O}$ mixture to the IR cell at 150 °C for 60 min in the dark when the intensities of adsorption

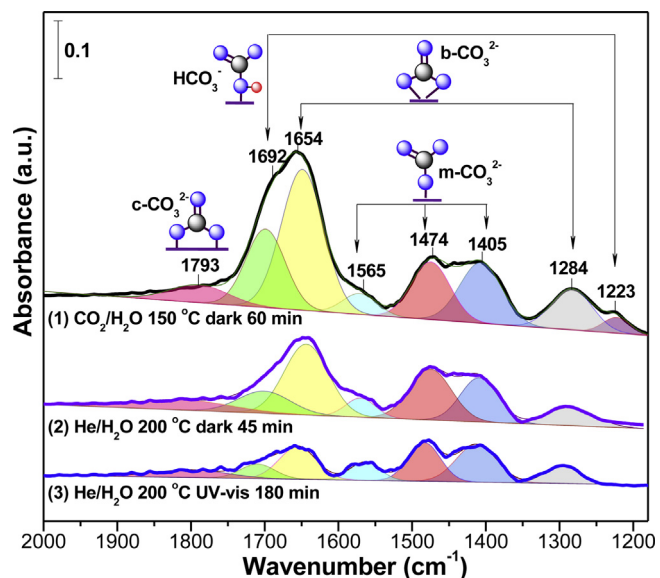


Fig. 9. In situ DRIFTS spectra for $\text{CO}_2 + \text{H}_2\text{O}$ adsorption (capture in the dark at 150 °C for 60 min) and intermediates desorption/transformation on MgAl/Ti₄₃ (at 200 °C in the dark by purging He + H_2O for 45 min and subsequently under UV-vis irradiation for 180 min at 200 °C).

peaks reached saturation or remained unchanged (Step 1). Next, to investigate the thermal effect on the desorption of surface species in the dark, the temperature was raised and maintained at 200 °C under a stream of He/H₂O for 45 min when the intensities of IR peaks remained unchanged (Step 2). Subsequently, the UV-vis light was turned on for 180 min to investigate the photocatalytic conversion of reaction intermediates and the desorption of products (Step 3). The in situ DRIFTS spectra recorded in each of the four steps are shown in Fig. 9.

As shown in Fig. 9 (spectrum 1), exposure of MgAl/Ti₄₃ to a $\text{CO}_2 + \text{H}_2\text{O}$ mixture resulted in a formation of intensive bidentate carbonate ($b\text{-CO}_3^{2-}$ at 1654 cm^{-1} and 1284 cm^{-1}) [14,46,48–50], moderate bicarbonate (HCO_3^- at 1692 cm^{-1} and 1223 cm^{-1}) and monodentate carbonate ($m\text{-CO}_3^{2-}$ at 1565 cm^{-1} , 1474 cm^{-1} , and 1405 cm^{-1}), and weak chelating bridged carbonate ($c\text{-CO}_3^{2-}$ at 1793 cm^{-1}) [14,16,49]. CO_2 interaction with MgAl(LDO) formed strong $b\text{-CO}_3^{2-}$ (at 1661 cm^{-1} and 1285 cm^{-1}), HCO_3^- (at 1710 cm^{-1} and 1222 cm^{-1}) but negligible $m\text{-CO}_3^{2-}$ (at 1517 cm^{-1} , 1464 cm^{-1} and 1394 cm^{-1}) (see Fig. S7, spectrum 1). The adsorbed species on MgAl/Ti₄₃ upon CO_2 adsorption were similar to those on MgAl(LDO) (the spectra are not shown here but the peak positions and intensities are summarized in Table 1). Our previous work also showed that CO_2 adsorption on TiO₂(P25) mainly led to the formation of HCO_3^- (at 1672 cm^{-1} and 1418 cm^{-1}) and $b\text{-CO}_3^{2-}$ (at 1545 cm^{-1} and 1340 cm^{-1}) [38]. Obviously, the peak positions of HCO_3^- , $b\text{-CO}_3^{2-}$ and $m\text{-CO}_3^{2-}$ on MgAl/Ti₄₃ were different from TiO₂ but close to MgAl(LDO), revealing that the adsorbed species on MgAl/Ti₄₃ were coordinated with MgAl(LDO) sites or MgAl/Ti interfacial sites. In general, the formation of HCO_3^- , $b\text{-CO}_3^{2-}$, $c\text{-CO}_3^{2-}$ and $m\text{-CO}_3^{2-}$ requires the participation of hydroxyl groups (OH), adjacent cationic site ($\text{M}^{n+}\text{-O}^{2-}$ pairs), $\text{M}^{n+}\text{-O}^{2-}$ and metal ion (M^{n+}), and oxygen ions (O^{2-}) with lowest coordination number [16,51], respectively. The stronger intensities of HCO_3^- , $b\text{-CO}_3^{2-}$, and $m\text{-CO}_3^{2-}$ than $c\text{-CO}_3^{2-}$ demonstrated that MgAl(Ti)-OH, MgAl(Ti)- O^{2-} and O^{2-} are the dominating adsorption sites for CO_2 capture on the surface of MgAl/Ti₄₃.

Fig. 9 also reveals that during the desorption step (spectrum 2), the peak intensities of HCO_3^- and $b\text{-CO}_3^{2-}$ substantially decreased by 53–68% but that of $c\text{-CO}_3^{2-}$ and $m\text{-CO}_3^{2-}$ only slightly changed by 15–17% (calculated by the peak intensity ratio of spectrum 2

Table 1

The peak position, peak intensity (normalized peak area), and peak intensity ratio of adsorbed species over MgAl/Ti₄₃, MgAl@Ti₄₃, and MgAl(LDO) samples.

Samples	Adsorbed species	Peak location (cm ⁻¹)	Intensity in spectrum 1 (I_1)	Intensity in spectrum 2 (I_2)	Intensity in spectrum 3 (I_3)	I_2/I_1	I_3/I_2
MgAl/Ti ₄₃	HCO ₃ ⁻	1692, 1223	9.7	3.1	1.2	0.32	0.40
	b-CO ₃ ²⁻	1654, 1284	21.1	9.9	3.1	0.47	0.31
	c-CO ₃ ²⁻	1793	2.7	2.1	1.2	0.83	0.56
	m-CO ₃ ²⁻	1565, 1474, 1405	15.1	12.8	8.2	0.85	0.64
MgAl@Ti ₄₃	HCO ₃ ⁻	1694, 1240	10.4	3.9	1.7	0.38	0.44
	b-CO ₃ ²⁻	1644, 1312	12.6	7.6	4.5	0.60	0.59
	c-CO ₃ ²⁻	1790	1.0	0.85	0.61	0.85	0.72
	m-CO ₃ ²⁻	1554, 1465	2.4	2.2	1.7	0.92	0.77
MgAl(LDO)	HCO ₃ ⁻	1710, 1222	8.8	6.4	5.8	0.73	0.91
	b-CO ₃ ²⁻	1661, 1285	9.5	8.3	8.0	0.87	0.96
	c-CO ₃ ²⁻	1785	1.6	1.5	1.4	0.94	0.93
	m-CO ₃ ²⁻	1517, 1464, 1394	2.0	1.8	1.7	0.90	0.94

to spectrum 1, as seen in **Table 1**). Subsequent UV-vis irradiation for 180 min induced not only a further decrease of residual HCO₃⁻ and b-CO₃²⁻ by 60–70% but also 35–45% desorption/conversion of strongly chemisorbed c-CO₃²⁻ and m-CO₃²⁻ (spectrum 3, and see the ratio of spectrum 3 to spectrum 2 in **Table 1**). The results indicate that it is easier and faster for b-CO₃²⁻ and HCO₃⁻ to desorb as CO₂ or transform into products (e.g., CO), likely due to the weaker base strength of OH and Mⁿ⁺–O²⁻ sites than strong-strength of O²⁻ sites [16,49]. By correlating the GC results in **Fig. 8** (condition II, thermal followed by photo-effect), we infer that (1) the majority of desorbed CO₂ due to thermal effect (dark process) is from weakly bonded HCO₃⁻ and b-CO₃²⁻, (2) the photocatalytic conversion product, CO, could originate from either weakly bonded HCO₃⁻, b-CO₃²⁻ or strongly bonded c-CO₃²⁻ and m-CO₃²⁻. It should be noted that no surface adsorbed CO (around 2100–2190 cm⁻¹) was observed by in situ DRFTS, probably because the photocatalytic process was done at 200 °C that induced easy desorption of CO. The facile desorption of product could be another advantage of our CCPC process.

To understand the difference in the desorption/conversion behavior of adsorbed species over MgAl/Ti₄₃, MgAl@Ti₄₃ and MgAl(LDO), we also calculated and compared the thermal-induced desorption and photo-induced conversion dynamics, as shown in **Table 1**. The adsorbed species on MgAl/Ti₄₃ tend to be more easily desorbed and converted than on MgAl@Ti₄₃ and bare MgAl(LDO). For example, during the desorption process HCO₃⁻ and b-CO₃²⁻ species on MgAl/Ti₄₃ desorbed by 53–68%, on MgAl@Ti₄₃ desorbed by 40–62%, while those on MgAl(LDO) only desorbed by 13–27%. Subsequent photo-illumination induced a decrease of all the adsorbed species by 35–70% on MgAl/Ti₄₃, by 28–55% on MgAl@Ti₄₃, but negligible changes on bare MgAl(LDO). Again, the in situ DRFTS results not only well explain why MgAl/Ti₄₃ is more active than MgAl@Ti₄₃, but also support the photocatalytic activity measurements that the hybrid MgAl/Ti materials are advantageous over bare MgAl(LDO) and TiO₂ for all three processes: CO₂ capture, desorption and conversion.

4. Conclusions

We have demonstrated a novel CCPC process and hybrid MgAl(LDO)/TiO₂ material to achieve high capacities of CO₂ adsorption/desorption and photocatalytic conversion to useful products, while regenerating the materials for following cycles without much energy input besides flue gas waste heat and solar energy. This unique hybrid materials, prepared by a combined hydrothermal and co-precipitation method, have well-crystallized and highly dispersed TiO₂ nanoparticles on the MgAl(LDO) nanoplates surface. In our CCPC route, MgAl(LDO)/TiO₂ acts as an adsorbent to capture CO₂ at a near-real flue gas temperature (~150 °C), and simultaneously works as a photocatalyst to convert the captured CO₂ into useful products at a high CO₂ conversion efficiency (10–15%)

at a moderate temperature (150~200 °C). Meanwhile, the hybrid material is automatically regenerated at the same temperature range (≤ 200 °C) with good capacity recovery. Furthermore, the produced CO and desorbed CO₂ can be economically separated by sequentially controlling the dark heating and photo-irradiation process. The CO₂ capture/conversion measurements combined with in situ DRFTS results demonstrated that (1) MgAl(LDO)/TiO₂ has higher adsorption capacity and desorption kinetics than bare MgAl(LDO), and (2) photo-illumination can activate and convert the strongly adsorbed species that cannot be achieved by thermal desorption alone at the same temperature. Findings in this work may lead to a promising and scalable technology to cut CO₂ emissions (with an add-on benefit of producing renewable fuels) in a more economical way than conventional CCS processes.

Acknowledgement

This work is supported by National Science Foundation (NSF) Early Faculty CAREER Award (CBET-1254709).

Appendix A. Supplementary data

Supplementary data associated with this article can be found, in the online version, at <http://dx.doi.org/10.1016/j.apcatb.2015.06.006>

References

- [1] N. Gargiulo, F. Pepe, D. Caputo, J. Nanosci. Nanotechnol. 14 (2014) 1811–1822.
- [2] N. MacDowell, N. Florin, A. Buchard, J. Hallett, A. Galindo, G. Jackson, C.S. Adjiman, C.K. Williams, N. Shah, P. Fennell, Energy Environ. Sci. 3 (2010) 1645–1669.
- [3] R.N.E. Huaman, T.X. Jun, Renew. Sustain. Energ. Rev. 31 (2014) 368–385.
- [4] S.D. Sharma, M. Azzi, Fuel 121 (2014) 178–188.
- [5] T.C. Merkel, X.T. Wei, Z.J. He, L.S. White, J.G. Wijmans, R.W. Baker, Ind. Eng. Chem. Res. 52 (2013) 1150–1159.
- [6] L. Dumee, C. Scholes, G. Stevens, S. Kentish, Int. J. Greenhouse Gas Control 10 (2012) 443–455.
- [7] A. Bandyopadhyay, Clean Technol. Environ. Policy 13 (2011) 269–294.
- [8] P.R. Gentry, T. House-Knight, A. Harris, T. Greene, S. Campleman, Int. Arch. Occup. Environ. Health 87 (2014) 591–606.
- [9] A. Garcia-Abuin, D. Gomez-Diaz, J.M. Navaza, J. Ind. Eng. Chem. 20 (2014) 2272–2277.
- [10] A. MacKenzie, D.L. Granatstein, E.J. Anthony, J.C. Abanades, Energy Fuels 21 (2007) 920–926.
- [11] A.M. Kierzkowska, R. Pacciani, C.R. Mueller, ChemSusChem 6 (2013) 1130–1148.
- [12] F.-C. Yu, N. Phalak, Z. Sun, L.-S. Fan, Ind. Eng. Chem. Res. 51 (2012) 2133–2142.
- [13] M. Broda, A.M. Kierzkowska, C.R. Mueller, ChemSusChem 5 (2012) 411–418.
- [14] X.P. Wang, J.J. Yu, J. Cheng, Z.P. Hao, Z.P. Xu, Environ. Sci. Technol. 42 (2008) 614–618.
- [15] R.V. Siriwardane, R.W. Stevens, Ind. Eng. Chem. Res. 48 (2009) 2135–2141.
- [16] M. Leon, E. Diaz, S. Bennici, A. Vega, S. Ordóñez, A. Auroux, Ind. Eng. Chem. Res. 49 (2010) 3663–3671.
- [17] A. Garcia-Gallastegui, D. Iruretagoyena, V. Gouvea, M. Mokhtar, A.M. Asiri, S.N. Basahel, S.A. Al-Thabaiti, A.O. Alyoubi, D. Chadwick, M.S.P. Shaffer, Chem. Mater. 24 (2012) 4531–4539.

[18] Y. Gao, Z. Zhang, J. Wu, X. Yi, A. Zheng, A. Umar, D. O'Hare, Q. Wang, J. Mater. Chem. A 1 (2013) 12782–12790.

[19] Z. Zhang, J. Wang, L. Huang, Y. Gao, A. Umar, Z. Huang, Q. Wang, Sci. Adv. Mater. 6 (2014) 1154–1159.

[20] M.J. Ramirez-Moreno, I.C. Romero-Ibarra, M.A. Hernandez-Perez, H. Pfeiffer, Ind. Eng. Chem. Res. 53 (2014) 8087–8094.

[21] S.W. Bian, J. Baltrusaitis, P. Galhotra, V.H. Grassian, J. Mater. Chem. 20 (2010) 8705–8710.

[22] A. Le Gal, S. Abanades, G. Flamant, Energy Fuels 25 (2011) 4836–4845.

[23] C.-J. Liu, J. Ye, J. Jiang, Y. Pan, ChemCatChem 3 (2011) 529–554.

[24] F. Studt, I. Sharafutdinov, F. Abild-Pedersen, C.F. Elkjaer, J.S. Hummelshoj, S. Dahl, I. Chorkendorff, J.K. Norskov, Nat. Chem. 6 (2014) 320–324.

[25] R.J. Lim, M. Xie, M.A. Sk, J.-M. Lee, A. Fisher, X. Wang, K.H. Lim, Catal. Today 233 (2014) 169–180.

[26] V.P. Indrakanti, J.D. Kubicki, H.H. Schobert, Energy Environ. Sci. 2 (2009) 745–758.

[27] L. Liu, Y. Li, Aerosol Air Qual. Res. 14 (2014) 453–469.

[28] E.V. Kondratenko, G. Mul, J. Baltrusaitis, G.O. Larrazabal, J. Perez-Ramirez, Energy Environ. Sci. 6 (2013) 3112–3135.

[29] A. Dhakshinamoorthy, S. Navalon, A. Corma, H. Garcia, Energy Environ. Sci. 5 (2012) 9217–9233.

[30] S.N. Habisreutinger, L. Schmidt-Mende, J.K. Stolarczyk, Angew. Chem. Int. Ed. 52 (2013) 7372–7408.

[31] C. Wang, R.L. Thompson, J. Baltrus, C. Matranga, J. Phys. Chem. Lett. 1 (2010) 48–53.

[32] W.-N. Wang, W.-J. An, B. Ramalingam, S. Mukherjee, D.M. Niedzwiedzki, S. Gangopadhyay, P. Biswas, J. Am. Chem. Soc. 134 (2012) 11276–11281.

[33] W.-N. Wang, J. Park, P. Biswas, Catal. Sci. Technol. 1 (2011) 593–600.

[34] X. Li, Z. Zhuang, W. Li, H. Pan, Appl. Catal. A Gen. 429 (2012) 31–38.

[35] S. Xie, Y. Wang, Q. Zhang, W. Fan, W. Deng, Y. Wang, Chem. Commun. 49 (2013) 2451–2453.

[36] L. Liu, F. Gao, H. Zhao, Y. Li, Appl. Catal. B Environ. 134 (2013) 349–358.

[37] J. Mao, L. Ye, K. Li, X. Zhang, J. Liu, T. Peng, L. Zan, Appl. Catal. B Environ. 144 (2014) 855–862.

[38] L. Liu, C. Zhao, H. Zhao, D. Pitts, Y. Li, Chem. Commun. 49 (2013) 3664–3666.

[39] L. Liu, C. Zhao, D. Pitts, H. Zhao, Y. Li, Catal. Sci. Technol. 4 (2014) 1539–1546.

[40] S.J. Han, Y. Bang, H.J. Kwon, H.C. Lee, V. Hiremath, I.K. Song, J.G. Seo, Chem. Eng. J. 242 (2014) 357–363.

[41] L. Liu, H. Zhao, J.M. Andino, Y. Li, ACS Catal. 2 (2012) 1817–1828.

[42] R. Lu, X. Xu, J. Chang, Y. Zhu, S. Xu, F. Zhang, Appl. Catal. B Environ. 111 (2012) 389–396.

[43] A.D. Ebner, S.P. Reynolds, J.A. Ritter, Ind. Eng. Chem. Res. 45 (2006) 6387–6392.

[44] A.D. Ebner, S.P. Reynolds, J.A. Ritter, Ind. Eng. Chem. Res. 46 (2007) 1737–1744.

[45] P.-H. Chang, T.-J. Lee, Y.-P. Chang, S.-Y. Chen, ChemSusChem 6 (2013) 1076–1083.

[46] D.A. Torres-Rodriguez, E. Lima, J.S. Valente, H. Pfeiffer, J. Phys. Chem. A 115 (2011) 12243–12250.

[47] M.K.R. Reddy, Z.P. Xu, G.Q. Lu, J.C.D. da Costa, Ind. Eng. Chem. Res. 47 (2008) 2630–2635.

[48] M.L. Baily, C. Chizallet, G. Costentin, J.M. Krafft, H. Lauron-Pernot, M. Che, J. Catal. 235 (2005) 413–422.

[49] H. Du, C.T. Williams, A.D. Ebner, J.A. Ritter, Chem. Mater. 22 (2010) 3519–3526.

[50] D. Cornu, H. Guesmi, J.M. Krafft, H. Lauron-Pernot, J. Phys. Chem. C 116 (2012) 6645–6654.

[51] W. Su, J. Zhang, Z. Feng, T. Chen, P. Ying, C. Li, J. Phys. Chem. C 112 (2008) 7710–7716.